3D-printed Ti/graphene composite current collectors for high-voltage aqueous zinc-ion batteries

Yang Zhiqiang[1], Yang Hao[1], Wang Rui[1,2,*], Wan Yi[1], Zhang Yan[1], Liu Chenhao[1], Zhang Zian[1], Li Yuqi[1], Wu Mingbo[1,3], Hu Han[1,*], Chen De[4,*]

(1. *State Key Laboratory of Heavy Oil Processing*, *Shandong Key Laboratory of Advanced Electrochemical Energy Storage Technologies*, *College of Chemistry and Chemical Engineering*, *China University of Petroleum (East China)*, *Qingdao* 266580, *China*;
2. *Key Laboratory of Advanced Energy Materials Chemistry (Ministry of Education)*, *Nankai University*, *Tianjin* 300071, *China*;
3. *College of Chemical Engineering*, *Qingdao University of Science&Technology*, *Qingdao* 266061, *China*;
4. *Department of Chemical Engineering*, *Norwegian University of Science and Technology*, *Trondheim* 7491, *Norway*)

Abstract: Aqueous zinc-ion batteries (AZIBs) have significant promise as large-scale energy storage devices due to their high safety, low cost, and environmental friendliness. However, their application has been constrained by limited operational voltage windows. A high-voltage-resistant Ti-graphene-Ti cathode current collector (TGT) was designed and fabricated by three-dimensional (3D) printing. The surface of the TGT has a Ti_xO_y protective layer, which effectively suppresses electrolyte decomposition under high voltage conditions so that the voltage window of the battery is extended to 1.0–2.2 V without the obvious formation of by-products. Simultaneously, the graphene layer in the TGT structure significantly improves the adsorption and insertion/extraction kinetics of cations, resulting in a high specific capacity of 307.5 mAh g^{-1} and a prolonged cycling life of the battery. The resultant AZIBs have a stable charge/discharge performance over 400 cycles at a high voltage. Furthermore, the influence of the geometric arrangements of Ti and graphene in the 3D printing process on the energy storage mechanism was investigated and provided novel insight for the development of high-voltage-resistant composite cathode current collectors for AZIBs.

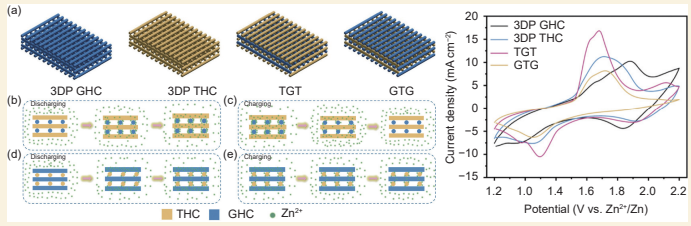

Key words: 3D printing; Aqueous zinc-ion batteries; Composite current collectors; High-voltage cathodes; Wide voltage window

1 Introduction

Aqueous zinc-ion batteries (AZIBs) are promising grid-scale energy storage devices because of their high safety, low cost and environment friendliness[1–11]. As a critical component of AZIBs, the current collector of cathode not only collects the current generated by active materials but also impacts the voltage window, cycle stability, and safety of batteries[12–17]. However, traditional Al or stainless steel current collectors are prone to corrosion in aqueous electrolytes, limiting the operating voltage range of AZIBs[18–20]. In contrast, corrosion-resistant Ti metal possesses low reactivity in electrolytes due to the presence of inert oxide layer on its surface[21]. When employed as current collectors, Ti metal can effectively suppress the electrochemical decomposition of water under high voltage and reduce the accumulation of by-products on the cathode surface[22–25]. Nevertheless, the limited specific surface area of Ti current collectors impedes their ability to effectively adsorb ions from the electrolyte[26]. When paired with manganese oxide active materials, the dissolved Mn^{2+} generated from manganese oxide dissolution cannot efficiently deposit onto the cathode surface, resulting in a rapid capacity fading during electrochemical cyc-

Received: December 11, 2025
Revised: February 25, 2026
Accepted: February 26, 2026

ling process[27].

Compared with corrosion-resistant metal, carbon nanomaterials such as carbon nanotubes or graphene, exhibit high specific surface area and unique electronic structure[28]. As a result, they can effectively adsorb Mn^{2+} from the electrolyte, which inhibits the dissolution and shuttle effect of manganese oxide cathode materials, thereby significantly extending the cycle life of AZIBs[29–34]. Therefore, Ti-carbon composite current collectors were researched and developed, which ingeniously combine the high corrosion resistance of Ti with the high specific surface area of carbon nanomaterials. Current research mainly focuses on basic fabrication processes and optimal Ti-carbon ratio, while usually neglecting the important factors such as spatial positioning matching and synergistic effects between the Ti and carbon nanomaterials, which directly determines the electron transport efficiency, ion migration capability, and cycling stability of current collectors[35–36]. Moreover, traditional preparation methods struggle to precisely control the microstructure of composite current collectors, limiting their application effectiveness in AZIBs.

In recent years, three-dimensional (3D) printing technology has emerged as an innovative electrode fabrication technique due to its flexibility, convenience, and high degree of controllability[37–41]. Through the layer-by-layer additive manufacturing principle, this technology can precisely control the spatial distribution and proportional relationship of Ti and carbon nanomaterials in composite current collectors. Herein, a Ti-graphene-Ti composite current collector (TGT) was fabricated by vertically interleaving stacked Ti metal and graphene oxide (GO) using 3D printing technology. The Ti-based outer layer of the TGT can suppress electrolyte decomposition under high voltage, thereby expanding the voltage window and minimizing the formation of by-product zinc hydroxysulfate (ZHS). Meanwhile, the graphene-based inner layer within the TGT structure enhances the adsorption and insertion/extraction kinetics of cations, resulting in an increased specific capacity of the cathode and extended the cycling life of AZIBs. Furthermore, the spatial configuration between Ti-based outer layer and graphene-based inner layer has been deeply investigated, revealing their synergistic mechanism on enhancing the electrochemical performance of cathodes. This work provides novel insights for the development of high-performance composite cathode current collectors for AZIBs.

2 Experimental

2.1 3D Printing of current collectors

The GO-hydroxypropyl methylcellulose (HPMC)-carbon nanotubes (CNTs) (GHC) ink was prepared by mixing 0.8 g of GO (Jiangsu XFNANO Materials Tech Co., Ltd.), 0.4 g of HPMC (Macklin), and 5 mL of 4.2% (mass fraction) CNTs dispersion (purchased from QingDao HaoXin New Energy Technology Co. Ltd.) in a planetary mixer (Thinky ARE-310) at 2000 r min^{-1} for 5 min. The Ti powder-HPMC-CNTs (THC) ink was prepared by mixing 2 g of Ti powder (300 mesh, Aladdin), 0.4 g of HPMC, and 3.8 mL of 4.2% CNTs dispersion in a planetary mixer at 2000 r min^{-1} for 5 min. The ink was transferred into a syringe barrel (5 mL) and centrifuged at 6000 r min^{-1} for 5 min. Then, it was 3D printed through a needle (410 μm in diameter) by a Bio-Architect@SR 3D printer, and the gap between 2 filaments was 1.2 mm. The printed layers are 5 in total. For TGT, odd layers use THC ink while even layers use GHC ink; for GTG, the arrangement is reversed. After the subsequent freeze-drying and heat treatment process (1100 °C for 2 h) in an inert atmosphere, the 3D-printed current collectors were prepared.

2.2 Electrodeposition of MnO_2 on 3D-printed current collectors

The electrodeposition of MnO_2 was operated in a three-electrode electrolytic device with 3D-printed current collectors as the working electrode, Pt foil as the counter electrode, saturated calomel electrode as the reference electrode in a mixed solution containing 0.1 mol L^{-1} $MnC_4H_6O_4$ and 0.1 mol L^{-1} Na_2SO_4 at a constant current density of 4 mA cm^{-2}. After 1 h and 20 min of electrodeposition, the MnO_2 loading on the 3D-printed current collectors was 11 mg cm^{-2}. After

electrodepositing, 3D-printed current collectors were cleaned with deionized water and dried at 35 °C in an oven overnight.

2.3 Characterization

X-ray diffraction (XRD) patterns were recorded by a X′ Pert PRO MPD diffractometer equipped with Cu *K*a radiation (λ = l.540 6 Å). X-ray photoelectron spectroscopy (XPS) was determined by a Thermo Fisher Scientific Escalab 250XI spectrometer with Al *K*α radiation. Scanning electron microscope (SEM) images and the corresponding elemental mapping were obtained from on ZEISS Sigma 300 equipped with energy dispersive X-ray spectroscopy systems. The nitrogen adsorption/desorption measurements were conducted on a Quantachrome Autosorb-iQ surface area analyzer. Raman spectra were recorded by a Renishaw Qontor confocal laser microscopy Raman spectrometer with an excitation wavelength of 532 nm. Rheological properties of inks were recorded by a HAAKE MARS 6000 rheometer.

2.4 Electrochemical measurement

Typical zinc-ions batteries composed of 3D-printed current collectors (loaded/unloaded MnO_2) and Zn foil as anode in an aqueous electrolyte with 2 mol L^{-1} $ZnSO_4$ and 0.1 mol L^{-1} $MnSO_4$ for zinc storage (for high-voltage galvanostatic charge-discharge testing, use 2 mol L^{-1} $ZnSO_4$, 0.1 mol L^{-1} $MnSO_4$, and 25 mmol L^{-1} 4-OH-TEMPO). Profiles including cyclic voltammetry (CV) and electrochemical impedance spectroscopy (EIS) were obtained on an Ivium stat electrochemical workstation while galvanostatic charge/discharge and cyclic performance of the ZIBs were recorded using the LAND CT2001A battery test system.

3 Results and discussion

3D-printed current collectors were fabricated by solidifying 2 functional inks according to a preset program. The GHC ink was prepared based on GO, HPMC, and CNTs. Simultaneously, the THC ink was prepared based on Ti powder, HPMC, and CNTs (Fig. S1 and Fig. S2). Through precisely controlling the ratio of the 2 inks and printing path planning, current collectors with different components and structures can be achieved (Fig. S3 and Fig. S4). The 3D-printed GHC-based current collectors (3DP GHC) and 3D-printed THC-based current collectors (3DP THC) were respectively prepared using pure GHC or THC inks, constructing homogeneous multi-layer structures. In contrast, the TGT and graphene-Ti-graphene current collectors (GTG) were fabricated by alternating printing of GHC and THC inks in the Z-direction (Fig. S5). Fig. S5 also shows the pore structure formed by crosslinking HPMC with graphene oxide/Ti powder. In the TGT structure, the outermost layer is composed of THC, while in the GTG structure, the outermost layer is composed of GHC. The schematic diagrams of these 4 types of current collectors are shown in Fig. 1a. Compared to other current collectors, TGT exhibits unique advantages. The Ti-containing outermost layer significantly enhances the mechanical strength of the current collector, enabling it to maintain an intact 3D structure under certain pressure (Fig. S6), which is beneficial for structural stability during long-term cycling. The hysteresis loops in the adsorption-desorption isotherms and the pore size distribution confirm that this composite collector is abundant in mesopores (Fig. S7). TEM images show the presence of mesopores (Fig. S8). The synergistic effect between the 3D porous network and the abundant oxygen-containing functional groups on its surface endows TGT with exceptional water wettability (Fig. S9). This facilitates rapid mass transfer at the cathode/electrolyte interface in aqueous electrolytes. Furthermore, the surface of TGT not only features an inert Ti_xO_y oxide film but also possesses abundant carbon defects provided by the GHC layer (Fig. S10 and Fig. S11), which is beneficial for improving charge transfer efficiency at the cathode/electrolyte interface[42].

The spatial distribution of components within composite current collectors exerts an important influence on cation adsorption behavior. Due to the significantly larger specific surface area and more abundant active sites of GHC, cations preferentially adsorb onto the graphene inner layer of the TGT structure

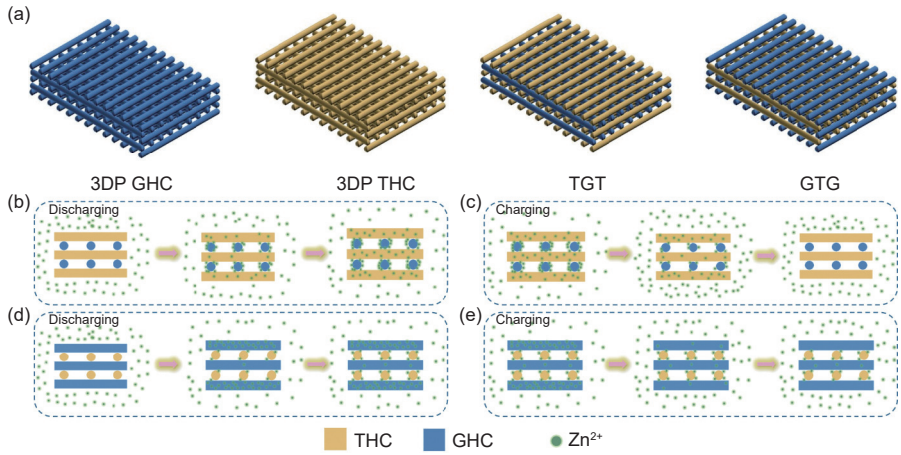

Fig. 1　(a) Schematic diagram of 3D-printed current collectors. Locations of Zn^{2+} in the TGT structure: (b) Discharging; (c) Charging. Locations of Zn^{2+} in the GTG structure: (d) Discharging; (e) Charging

during electrochemical processes (Fig. 1b–e). This selective adsorption mechanism effectively prevents excessive cation accumulation on the electrode surface, thereby suppressing charge shielding effects. MnO_2 active material was fabricated on the TGT current collector by electrodeposition, achieving a high loading capacity of approximately 11 mg cm^{-2}. Owing to the 3D conductive network structure of TGT, the current collector displays highly uniform current distribution (Fig. S12). Thus, MnO_2 nanoparticles are uniformly distributed over the entire 3D current collector surface, forming a continuous and dense active layer (Fig. S13). XRD analysis reveals that the prepared MnO_2 exhibits excellent consistency with the characteristic peaks of ε-MnO_2 phase (Fig. S14). More importantly, XPS analysis of the Mn 2p orbital fine structure shows that the spin-orbit splitting width between Mn $2p_{1/2}$ and Mn $2p_{3/2}$ is 11.70 eV, which aligns closely with the typical values of reported MnO_2 (Fig. S15)[43], further confirming the successful loading of ε-MnO_2.

The CV curves of several collector materials all exhibit 2 pairs of redox peaks, corresponding to the dual-ion mechanism of H^+ and Zn^{2+} (Fig. S16). Owing to the exquisite design and multi-layer synergistic effects of the TGT structure, the TGT cathode exhibits excellent electrochemical performance. At a low current density of 0.1 mA cm^{-2}, the areal specific capacity of TGT cathode reaches 3.1 mAh cm^{-2} (Fig. 2a), corresponding to a mass-specific capacity of 307.5 mAh g^{-1} (Fig. S17). When the current density increases to 0.5 mA cm^{-2} and then restored to 0.1 mA cm^{-2}, the areal capacity maintains at 2.6 mAh cm^{-2} (Fig. 2b), which consistently exceeds those of cathodes based on other 3D current collectors or conventional titanium mesh (Fig. S18). The electrode interfacial properties can be analyzed through electrochemical impedance spectroscopy (EIS). The plots reveal that the TGT cathode (R_{ct} = 617.3 Ω) exhibits a reduced semicircle diameter in the high-frequency region (Fig. 2c and Table S1), indicating its low charge transfer resistance, suggesting rapid electron transport. After 700 charge/discharge cycles, the TGT cathode maintains its specific capacity of 87.8 mAh g^{-1} (Fig. 2d), demonstrating a retention rate of 92.8%. It is noteworthy that some cycling curves exhibited a pattern of initial decline followed by recovery. The dissolution of MnO_2 caused a decrease in specific capacity, while the addition of $MnSO_4$ to the electrolyte supplied Mn^{2+} ions. The dissolution of Mn^{2+} gradually restored the specific capacity. Galvanostatic Intermittent Titration Technique (GITT) test (Fig. S19) results indicate that the diffusion coefficient of TGT ranges between 10^{-4} and 10^{-9} cm^2 s^{-1} at all voltages. This confirms the fast ion transport behavior of TGT. Further Raman characterization of the cycled cathodes revealed that the TGT surface exhibits no obvious characteristic peak related to ZHS (Fig. S20). While 3DP GHC exhibits a Zn^{2+}-OSO_3^{2-} related peak at 422.4 cm^{-1}, along with SO_4^{2-} related peaks at

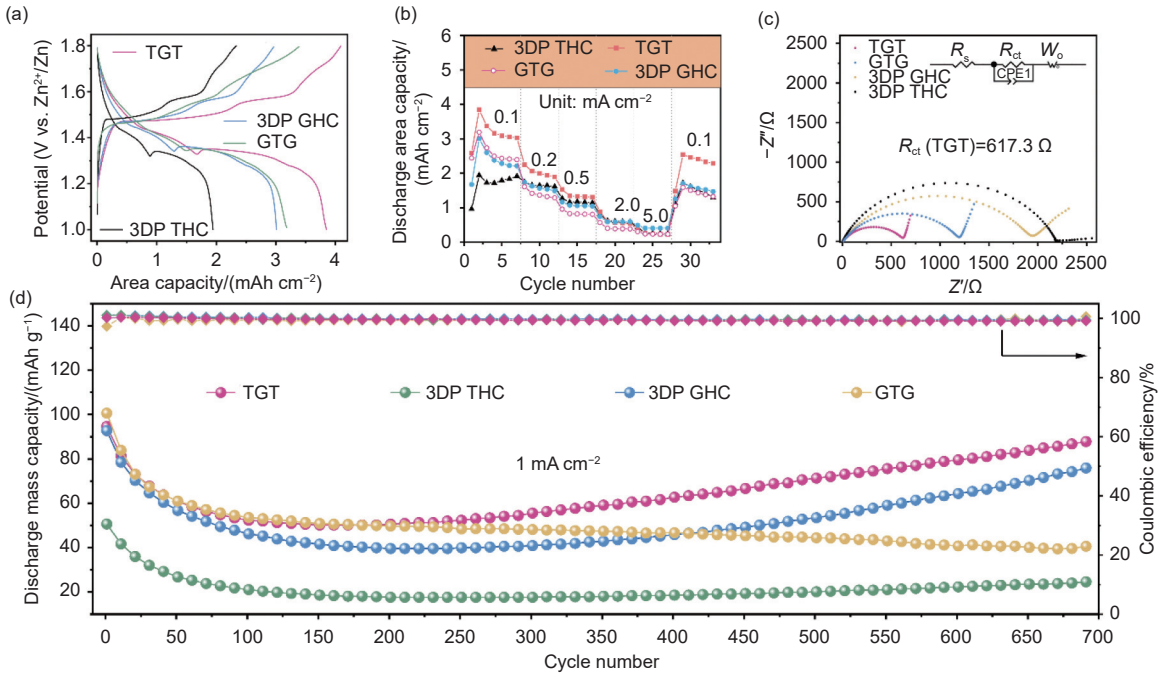

Fig. 2 Electrochemical performance of MnO_2 cathode based on TGT, GTG, 3DP GHC and 3DP THC: (a) Galvanostatic charge-discharge curves. (b) Rate performance. (c) Nyquist plots. (d) Cyclic stability and Coulombic efficiency

1026.0, 1081.4 and 1185.9 cm^{-1}, indicating a generation of ZHS[44]. In addition, the Zn anode showed no significant change after 700 cycles, which contributes to the long-term stable cycling of the batteries (Fig. S21).

Furthermore, the Ti_xO_y layer formed on the outer surface of the TGT effectively suppresses the oxygen evolution reaction of water molecules in electrolyte through physical barrier effect and chemical passivation. This suppression significantly broadens the electrochemical stability window of the battery, extending the operational voltage range from the conventional 0–2.0 to 0–2.4 V. The CV tests at different voltage ranges clearly demonstrate that Ti-based current collectors, including TGT, GTG and 3DP THC, exhibit no significant oxygen evolution peak within 0–2.4 V (Fig. 3a–d). However, the GHC current collector displays an obvious oxygen evolution plateau at 2.4 V. Furthermore, the increasing ratio of GHC would exacerbate the polarization of batteries (Fig. 3e–f, Fig. S22–S24). To further verify the electrochemical performance of TGT under high-voltage conditions, 2,2,6,6-tetramethylpiperidinyl-1-oxide (TEMPO) was introduced into traditional electrolyte which is a highly efficient redox mediator and can provide additional charging plateaus (Fig. S25–S26) [45]. During cycling at various current densities, the TGT demonstrates higher specific capacity and longer cycle life (over 400 cycles) (Fig. 3g–h). This is attributed to the synergistic mechanism of TGT, where the inner GHC layer, with its abundant active sites, preferentially undergoes electrochemical reactions, preventing the rapid consumption of TEMPO at the electrode surface. Simultaneously, the spatial protection effect of the outer THC layer further suppresses the decomposition of electrolyte, ensuring long-term stability of the electrode/electrolyte interface, thereby achieving a synergistic enhancement of energy density and cycling stability under high-voltage conditions. GTG exhibits a sharp capacity drop due to rapid depletion of surface TEMPO (Fig. S27). Upon losing the additional discharge plateau provided by TEMPO, the Coulombic efficiency recovers to approximately 100%.

In order to further investigate the synergistic mechanism between GHC and THC within the TGT current collector, the electrochemical kinetic characterization was carried out through CV tests at different scan rates. The CV curves clearly display 4 characteristic redox peaks (Fig. 4a, 4d). Peaks 1 and 4 corresponded to the insertion/extraction process of H^+,

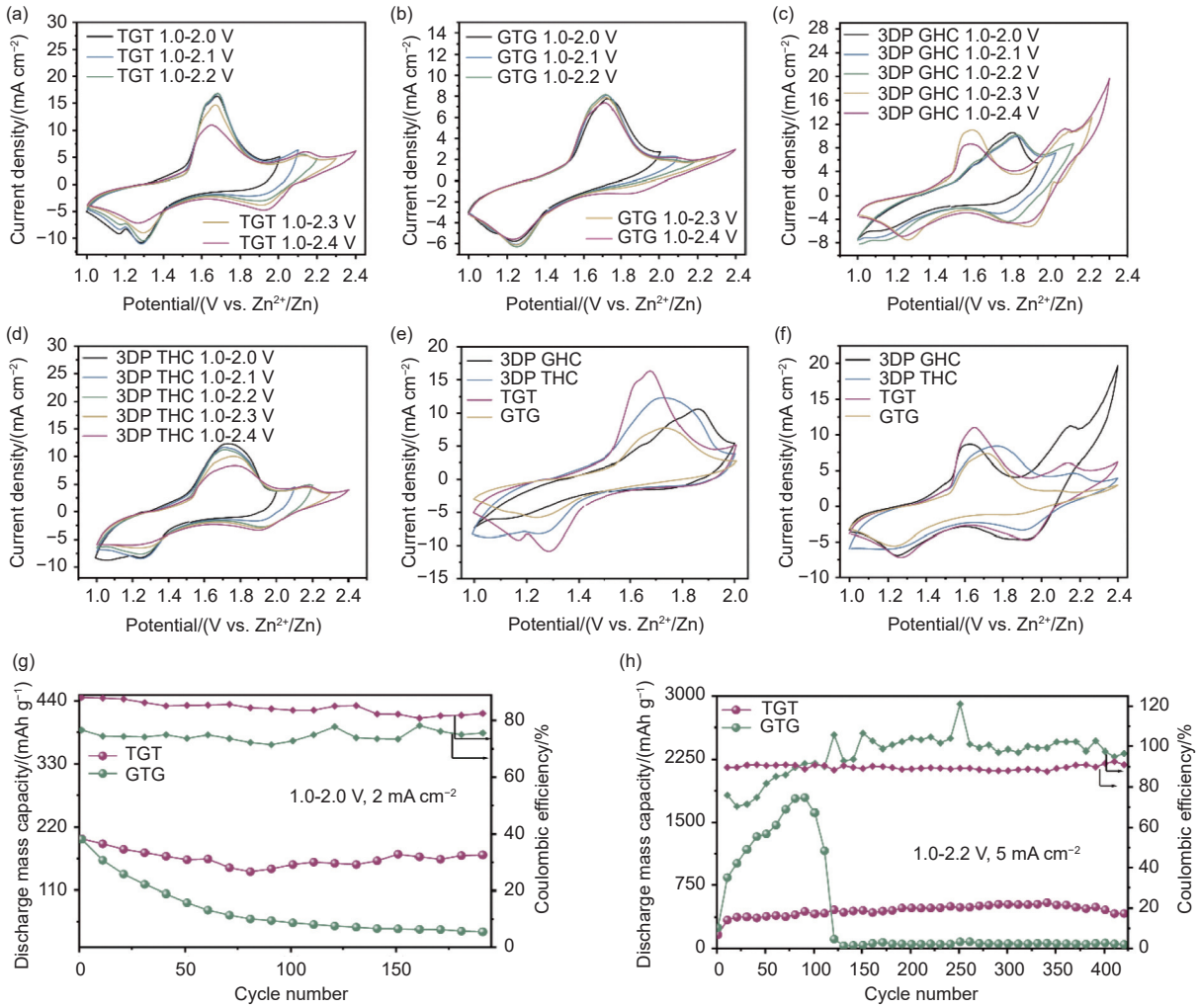

Fig. 3　CV curves of 3D-printed current collectors at voltage ranges from 1.0–2.0 V to 1.0–2.4 V: (a) TGT. (b) GTG. (c) 3DP GHC. (d) 3DP THC. CV curves of 3D-printed current collectors in the voltage range of (e) 1.0–2.0 V and (f) 1.0–2.4 V. Cycle performance of TGT and GTG under (g) 1.0–2.0 V, 2 mA cm^{-2} and (h) 1.0–2.2 V, 5 mA cm^{-2}

while peaks 2 and 3 represented the reversible insertion/extraction behavior of Zn^{2+}[46]. The *b* values of peaks 1, 2, 3 and 4 for 3DP GHC are 0.47, 0.62, 0.61 and 0.38, respectively (Fig. 4b), while those for 3DP THC are 0.53, 0.44, 0.45 and 0.42, respectively (Fig. 4e). Notably, the *b* values of 3DP GHC for Zn^{2+} insertion/extraction processes are higher than those of 3DP THC, which directly demonstrate that the GHC structure possesses superior Zn^{2+} transport kinetics. Further capacitive contribution quantification showed that 3DP GHC consistently exhibited higher capacitive contribution ratios than 3DP THC at different scan rates (Fig. 4c, 4f), which is consistent with the b-value result. To deeply verify the kinetic results, ex-situ Raman spectroscopy characterization was performed on 3DP GHC and 3DP THC during charge-discharge processes (Fig. 4g). The Raman spectra revealed 4 characteristic peaks: V_1 (510.3 cm^{-1}), V_2 (575.0 cm^{-1}), V_3 (681.2 cm^{-1}), and V_4 (992.8 cm^{-1}). Among these, V_1, V_2 and V_3 primarily originated from interlayer Zn^{2+} insertion/extraction, while V_4 corresponded to the tunneling insertion/ extraction of Zn^{2+}[47]. The V_4 peak of 3DP GHC become clearly visible upon discharge to 1.2 V and almost completely disappeared upon charge to 1.4 V (Fig. 4h). In contrast, the V_4 peak of 3DP THC only become apparent upon discharge to 1.0 V and is barely eliminated until charge to 1.6 V (Fig. 4i). This phenomenon strongly confirms that the electrochemical reaction kinetic on 3DP GHC surface is significantly faster than that on 3DP THC.

In addition to electrochemical kinetic characteristics, GHC and THC in the TGT structure also exhib-

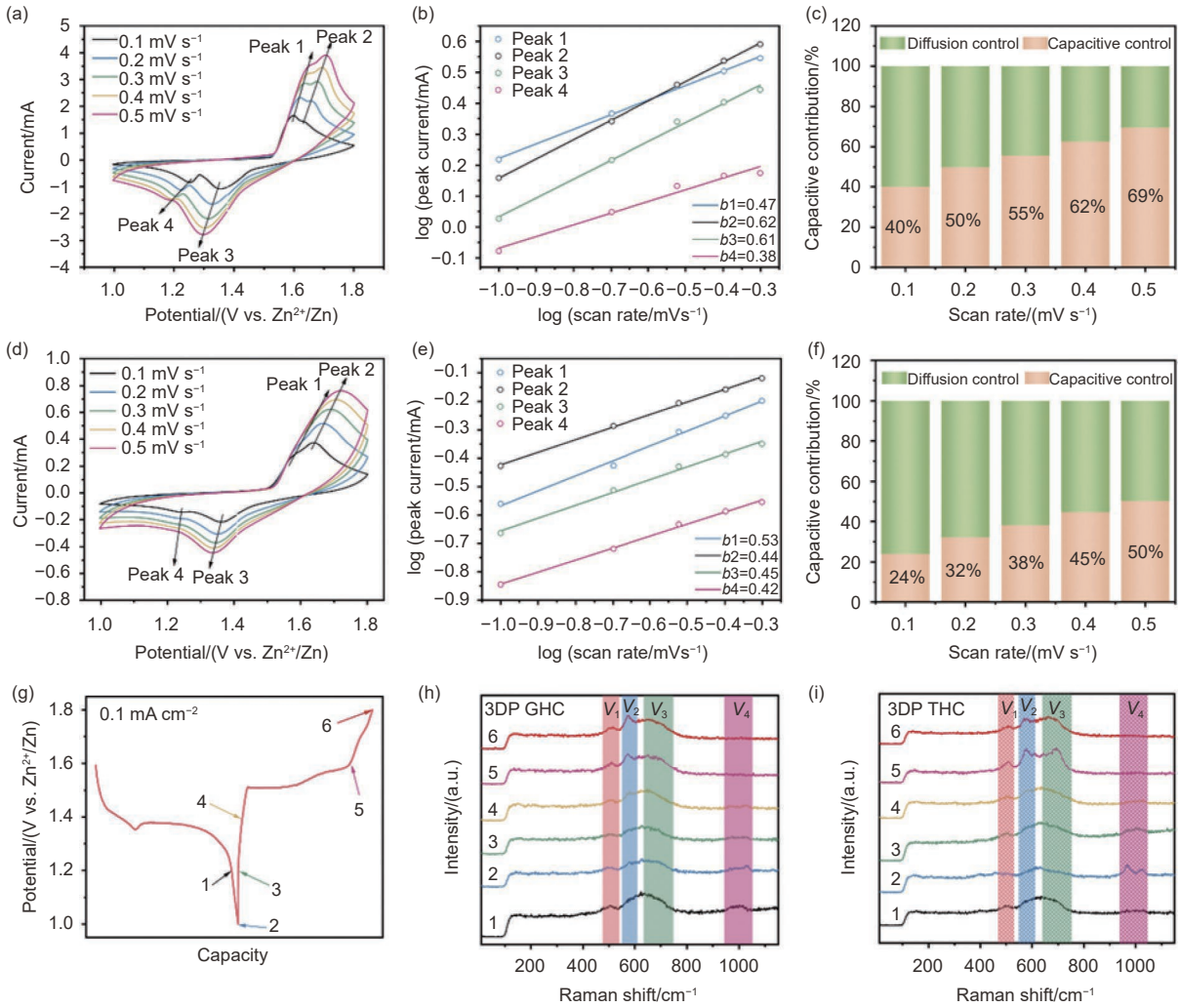

Fig. 4 Variable sweep speed CV test for 3DP GHC: (a) CV curves of diverse sweep rates; (b) log *i* versus log *v* plots at 4 peaks; (c) corresponding percentage of capacitive contribution. Variable sweep speed CV test for 3DP THC: (d) CV curves of diverse sweep rates; (e) log *i* versus log *v* plots at 4 peaks; (f) corresponding percentage of capacitive contribution. (g) Galvanostatic charge-discharge curves. Ex-situ Raman spectra of (h) 3DP GHC and (i) 3DP THC

it synergistic effects in suppressing the by-product formation and inducing deposition of Mn^{2+}. The cycling tests were conducted within 0.5–1.0 V at a current density of 1 mA cm^{-2}, which reveals that the 3DP GHC consistently maintains a high areal specific capacity (Fig. 5a), while the capacity from the 3DP THC is nearly negligible. The XPS was utilized to characterize the chemical state evolution on the surfaces of 3DP GHC and 3DP THC before and after cycling. 3DP GHC displays distinct S 2p and Zn $2p_3$ characteristic signals after cycling (Fig. 5b). High-resolution S 2p spectra clearly displayed an S $2p_{3/2}$ peak at 171.15 eV and an S $2p_{1/2}$ peak at 169.6 eV (Fig. 5c), which indicate the presence of SO_4^{2-}. Simultaneously, high-resolution Zn 2p XPS spectra show two characteristic peaks for Zn $2p_{1/2}$ and Zn $2p_{3/2}$ at 1045.4 and 1022.4 eV, respectively (Fig. S28), with a spin-orbit splitting energy of 23 eV[48]. This is entirely consistent with the theoretical value for Zn (II) species, confirming the formation of ZHS on the 3DP GHC surface. In contrast to 3DP GHC, XPS analysis of 3DP THC displays inapparent S signal, suggesting that the formation of by-products is suppressed.

To investigate the deposition behavior of Mn^{2+} on GHC and THC in the TGT and its impact on electrochemical performance, CV curves with different voltage range were conducted on 3DP GHC and 3DP THC (Fig. S29–S30). The 3DP GHC and 3DP THC both exhibit rectangular CV curves within the low-voltage range (1.0-1.6 V), reflecting typical double-

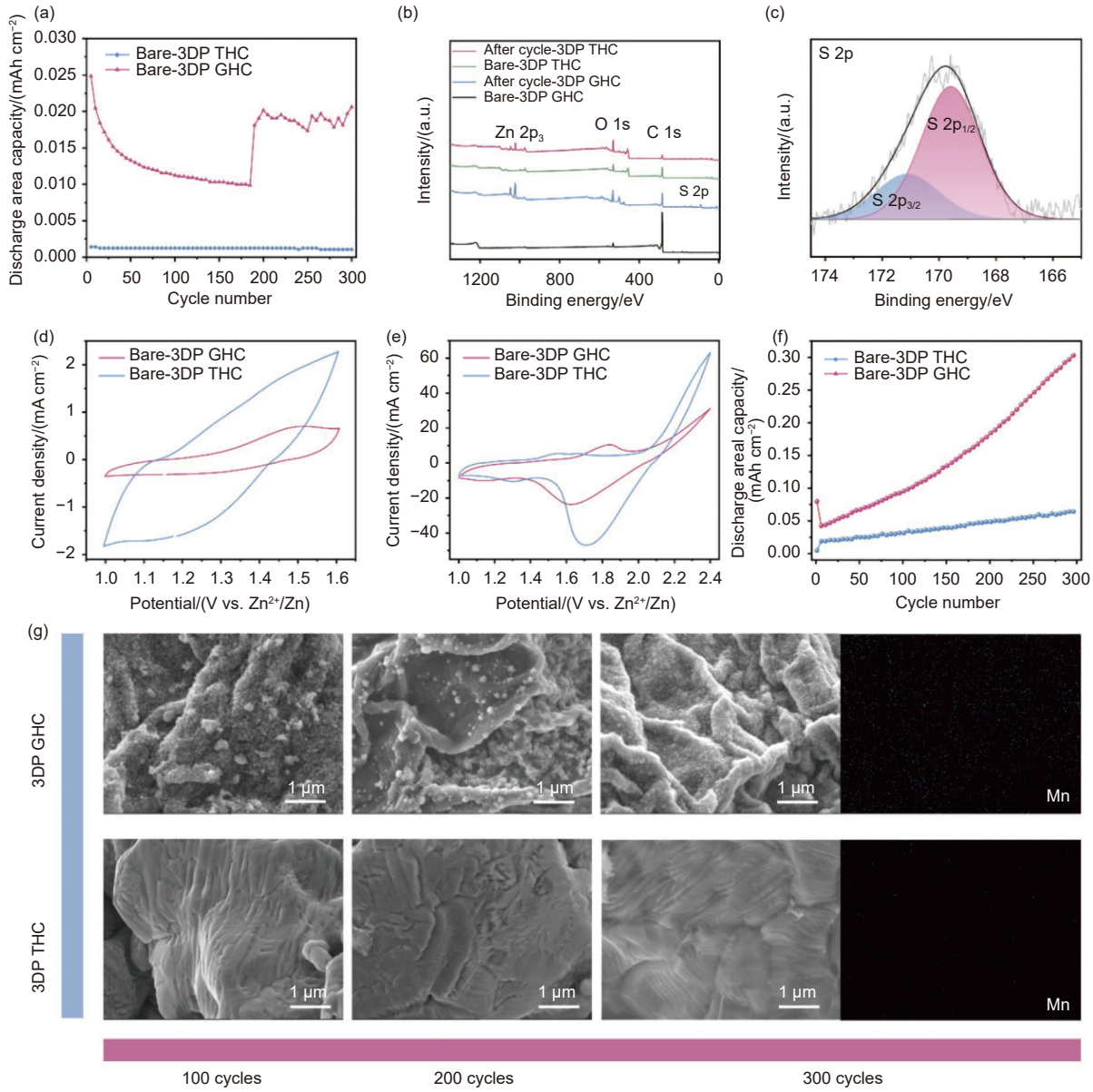

Fig. 5　(a) Cycling performance of bare 3DP GHC and 3DP THC at 0.5–1 V, 1 mA cm^{-2}. (b) XPS spectra of bare 3DP GHC and 3DP THC. (c) High-resolution S 2p XPS spectrum of 3DP GHC. CV curves (50 mV s^{-1}) of bare 3DP GHC and 3DP THC in the voltage range of (d) 1.0–1.6 V and (e) 1.0–2.4 V. (f) Cycling performance of bare 3DP GHC and 3DP THC at 1.0–2 V; 5 mA cm^{-2}. (g) SEM images of 3DP GHC and 3DP THC surface after cycling

layer capacitance-dominated electrochemical behavior (Fig. 5d). When the voltage range was extended to 1.0-2.4 V, 3DP GHC show a clear pair of redox peaks (Fig. 5e), while 3DP THC exhibited only a single reduction peak. This indicates that Mn^{2+} ions have deposited and have formed MnO_2 deposition layer on the 3DP GHC surface, thereby providing substantial pseudocapacitive contribution. After 300 charge/discharge cycles, the areal capacity of 3DP GHC can achieve 0.303 mAh cm^{-2} (Fig. 5f and Fig. S31), while the areal capacity of 3DP THC is merely 0.064 mAh cm^{-2}. This confirms the continuous deposition behavior of Mn^{2+} on 3DP GHC, which enhances the specific capacity of cathode. This result can also be proved by the morphology characterization of current collectors after cycling. The scanning electron microscope (SEM) images of cycled 3DP GHC shows uniformly distributed MnO_2 nanoparticles on its surface (Fig. 5g), whereas 3DP THC maintained a smooth morphology even after the same cycling conditions, with almost no detectable Mn deposition. This different surface evolution behavior reveals the fundament-

al differences in Mn^{2+} deposition kinetics between GHC and THC, providing crucial insights into the influence mechanisms of current collector selection on battery performance within the TGT structure.

4 Conclusion

In summary, a composite cathode current collector TGT was fabricated using 3D printing technology. The TGT consists of a THC outer layer and a GHC inner layer, forming a unique sandwich structure. Since the Ti_xO_y passivation layer formed on the surface, THC outer layer effectively suppresses electrolyte decomposition under high voltage. Meanwhile, the formation of ZHS by-products at the electrode interface is also reduced. Furthermore, the GHC layer in TGT possesses high specific surface area and abundant oxygen-containing functional groups, which significantly enhances the interfacial adsorption rate and insertion/extraction kinetics of Mn^{2+}. Therefore, the MnO_2 cathode based on TGT exhibits exceptional specific capacity of 307.5 mAh g^{-1}. Notably, this electrode maintains 400 stable cycles under high voltage range. This excellent cycling stability can be attributed to the synergistic mechanism between THC and GHC in the TGT structure. The THC outer layer acts as a protective barrier to effectively suppress interfacial side reactions, while the GHC inner layer serves as an active reaction center to promote the directional deposition and efficient conversion of Mn^{2+}, collectively establishing a stable electrode-electrolyte interface. This work provides theoretical guidance for the design of high-performance composite cathode current collectors, which is expected to advance the industrialization process of AZIBs.

Acknowledgements

The authors acknowledge the financial support from National Natural Science Foundation of China (22179145), Shandong Provincial Natural Science Foundation (ZR2023LFG005), Qingdao Natural Science Foundation (24-8-4-zrjj-5-jch), and Science and Technology Park Incubation Program Project of Qingdao City (25-1-1-yqpy-33-qy).

References

[1] Yan M, Ni H, Pan H. Rechargeable mild aqueous zinc batteries for grid storage[J]. Advanced Energy and Sustainability Research, 2020, 1(1): 2000026.

[2] Bensalah N, De Luna Y. Recent progress in layered manganese and vanadium oxide cathodes for Zn-ion batteries[J]. Energy Technology, 2021, 9(5): 2100011.

[3] Shang Y, Kundu D. A path forward for the translational development of aqueous zinc-ion batteries[J]. Joule, 2023, 7(2): 244-250.

[4] Wang D, Tang Y, Peng H, et al. Functional electrolyte additives for aqueous zinc-ion batteries: Progress and perspectives[J]. ChemSusChem, 2025, 18(19): e202501387.

[5] Tang B, Shan L, Liang S, et al. Issues and opportunities facing aqueous zinc-ion batteries[J]. Energy & Environmental Science, 2019, 12(11): 3288-3304.

[6] Fang G, Zhou J, Pan A, et al. Recent advances in aqueous zinc-ion batteries[J]. ACS Energy Letters, 2018, 3(10): 2480-2501.

[7] Lv W, Liu J, Shen Z, et al. Novel approaches to aqueous zinc-ion batteries: Challenges, strategies, and prospects[J]. eScience, 2025: 100410.

[8] Liu B, Xu Z, Wei C, et al. Re-understanding and mitigating hydrogen release chemistry toward reversible aqueous zinc metal batteries[J]. eScience, 2025, 5(3): 100330.

[9] Hou Z, He W, Wu F, et al. Tuning π-π carbon restacking hindrance to remodify hard carbon crystallites for advanced sodium energy[J]. Energy Storage Materials, 2025: 104455.

[10] Wu F, Zhao Y, Hou Z, et al. Lignocellulosic oxidation bridging to modulate pseudographitic domain of hard carbon toward boosted sodium storage[J]. Journal of Energy Storage, 2025, 130: 117496.

[11] Luo Z, Sun H, Zhao Y, et al. Separator engineering for high-energy rechargeable metal batteries: Fundamentals, design strategies and perspectives[J]. Energy Storage Materials, 2025: 104421.

[12] Ni Q, Kim B, Wu C, et al. Non-electrode components for rechargeable aqueous zinc batteries: Electrolytes, solid-electrolyte-interphase, current collectors, binders, and separators[J]. Advanced Materials, 2022, 34(20): 2108206.

[13] Huimin J, Chunlin X, Qi Z, et al. Anode current collector for aqueous zinc-ion batteries: Issues and design strategies[J]. Acta Chimica Sinica, 2023, 81(1): 29.

[14] Wang M, Wang W, Meng Y, et al. Crystal facet correlated Zn growth on Cu for aqueous Zn metal batteries[J]. Energy Storage Materials, 2023, 56: 424-431.

[15] Xiao X, Greenburg L C, Li Y, et al. Epitaxial electrodeposition of zinc on different single crystal copper substrates for high performance aqueous batteries[J]. Nano Letters, 2025, 25(4): 1305-1313.

[16] Shi S, Zhou D, Jiang Y, et al. Lightweight Zn-philic 3d-Cu scaffold for customizable zinc ion batteries[J]. Advanced Functional Materials, 2024, 34(24): 2312664.

[17] Li H, Li L, Liu W, et al. Recent advances in current collectors for aqueous zinc-ion batteries[J]. Chemical Record, 2025, 25(3): e202400217.

[18] Becknell N, Lopes P P, Hatsukade T, et al. Employing the dynamics of the electrochemical interface in aqueous zinc-ion battery cathodes[J]. Advanced Functional Materials, 2021, 31(35): 2102135.

[19] Liu B, Lv T, Zhou A, et al. Aluminum corrosion–passivation regulation prolongs aqueous batteries life[J]. Nature Communications, 2024, 15(1): 2922.

[20] Wu G, Yang Y, Zhu R, et al. The pitfalls of using stainless steel (SS) coin cells in aqueous zinc battery research[J]. Energy & Environmental Science, 2023, 16(10): 4320-4325.

[21] Terzi F, Dossi N. Ti as an electrode material. How to make the future better than the present[J]. Analytical and Bioanalytical Chemistry, 2015, 407(24): 7257-7261.

[22] Yu J, Yu C, Guo W, et al. Insight into the effects of current collectors and in situ Ni leaching in high-voltage aqueous supercapacitors[J]. Advanced Functional Materials, 2022, 32(34): 2204609.

[23] Zhao Y, Guo S, Chen M, et al. Tailoring grain boundary stability of zinc-titanium alloy for long-lasting aqueous zinc batteries[J]. Nature Communications, 2023, 14(1): 7080.

[24] Tian F, Wang F, Nie W, et al. Tailoring oxygen-depleted and unitary $Ti_3C_2T_x$ surface terminals by molten salt electrochemical etching enables dendrite-free stable Zn metal anode[J]. Angewandte Chemie International Edition, 2024, 63(36): e202408996.

[25] Li X, Li Q, Hou Y, et al. Toward a practical Zn powder anode: $Ti_3C_2T_x$ MXene as a lattice-match electrons/ions redistributor[J]. ACS Nano, 2021, 15(9): 14631-14642.

[26] Zhang G, Zhou W, Chen M, et al. Stainless steel foil: A more appropriate current collector than titanium foil for the cathodes of aqueous zinc ion batteries[J]. Electrochimica Acta, 2023, 437: 141519.

[27] Yang H, Wan Y, Sun K, et al. Reconciling mass loading and gravimetric performance of MnO_2 cathodes by 3d-printed carbon structures for zinc-ion batteries[J]. Advanced Functional Materials, 2023, 33(26): 2215076.

[28] Zheng J, Bock D C, Tang T, et al. Regulating electrodeposition morphology in high-capacity aluminium and zinc battery anodes using interfacial metal–substrate bonding[J]. Nature Energy, 2021, 6(4): 398-406.

[29] Khamsanga S, Pornprasertsuk R, Yonezawa T, et al. δ-MnO_2 nanoflower/graphite cathode for rechargeable aqueous zinc ion batteries[J]. Scientific Reports, 2019, 9(1): 8441.

[30] Lin D, Li J, Wang M, et al. Nanofluidic-engineered carbon nanotube ion highways in hydrogels enable high-power aqueous zinc-ion batteries[J]. Science Advances, 2025, 11(47): eadx9812.

[31] Chen M, Ma J, Feng Y, et al. Advancing aqueous zinc-ion batteries with carbon dots: A comprehensive review[J]. EcoEnergy, 2025, 3(2): 254-295.

[32] Wu L, Li X, Lu G, et al. Carbon quantum dot-assisted VO_2 (D) welding on holey graphene for zinc-ion battery cathode materials[J]. Journal of Electroanalytical Chemistry, 2024, 953: 118006.

[33] Xi M, Liu Z, Wang W, et al. Shear-flow induced alignment of graphene enables the closest packing crystallography of the (002) textured zinc metal anode with high reversibility[J]. Energy & Environmental Science, 2024, 17(9): 3168-3178.

[34] Li Y, Wu L, Dong C, et al. Manipulating horizontal Zn deposition with graphene interpenetrated Zn hybrid foils for dendrite-free aqueous zinc ion batteries[J]. Energy & Environmental Materials, 2023, 6(5): e12423.

[35] Li Z, Yi H, Li X, et al. Enhancing the cycling and rate performance of Ni-rich cathodes for lithium-ion batteries by bulk-phase engineering and surface reconstruction[J]. ACS Applied Materials & Interfaces, 2024, 16(22): 28537-28549.

[36] Cao H, Zhang Y, Zhou X, et al. Boosting the electrochemical performance of the Ni-rich $LiNi_{0.96}Co_{0.02}Mn_{0.02}O_2$ cathode by high-valence Zr/Mo dual-doping[J]. Chemical Communications, 2024, 60(98): 14629-14632.

[37] Zeng L, Ling S, Du D, et al. Direct ink writing 3D printing for high-performance electrochemical energy storage devices: A minireview[J]. Advanced Science, 2023, 10(32): 2303716.

[38] Saadi M, Maguire A, Pottackal N T, et al. Direct ink writing: A 3D printing technology for diverse materials[J]. Advanced Materials, 2022, 34(28): 2108855.

[39] Fina F, Goyanes A, Gaisford S, et al. Selective laser sintering (SLS) 3D printing of medicines[J]. International Journal of Pharmaceutics, 2017, 529(1-2): 285-293.

[40] Reyes C, Somogyi R, Niu S, et al. Three-dimensional printing of a complete lithium ion battery with fused filament fabrication[J]. ACS Applied Energy Materials, 2018, 1(10): 5268-5279.

[41] Cohen E, Menkin S, Lifshits M, et al. Novel rechargeable 3D-microbatteries on 3D-printed-polymer substrates: Feasibility study[J]. Electrochimica Acta, 2018, 265: 690-701.

[42] Guan L, Hu H, Li L, et al. Intrinsic defect-rich hierarchically porous carbon architectures enabling enhanced capture and catalytic conversion of polysulfides[J]. ACS Nano, 2020, 14(5): 6222-6231.

[43] Liang G, Mo F, Li H, et al. A universal principle to design reversible aqueous batteries based on deposition–dissolution mechanism[J]. Advanced Energy Materials, 2019, 9(32): 1901838.

[44] Aliahmadi F, Seifzadeh D, Samadianfard R, et al. Incorporation of zinc hydroxide sulphate (ZHS) nanoplates into epoxy resin to improve its corrosion protection[J]. Minerals, 2023, 13(2): 180.

[45] Jiang S, Xie Y, Xie Y, et al. Lewis acid-induced reversible disproportionation of tempo enables aqueous aluminum radical batteries[J]. Journal of the American Chemical Society, 2023, 145(26): 14519-14528.

[46] Sun W, Wang F, Hou S, et al. Zn/MnO_2 battery chemistry with H^+ and Zn^{2+} coinsertion[J]. Journal of the American Chemical Society, 2017, 139(29): 9775-9778.

[47] Zhang Y, Cui X, Liu Y, et al. Aqueous Zn-MnO_2 battery: Approaching the energy storage limit with deep Zn^{2+} pre-intercalation and revealing the ions insertion/extraction mechanisms[J]. Journal of Energy Chemistry, 2022, 67: 225-232.

[48] Liu A, Wu F, Zhang Y, et al. Insight on cathodes chemistry for aqueous zinc-ion batteries: From reaction mechanisms, structural engineering, and modification strategies[J]. Small, 2022, 18(28): 2201011.